



Deposited via The University of Leeds.

White Rose Research Online URL for this paper:

<https://eprints.whiterose.ac.uk/id/eprint/118391/>

Version: Accepted Version

Article:

Yousef, BM, Almarzooq, H, Angus, DA et al. (2017) Fracture parameter inversion from passive seismic shear-wave splitting: A validation study using full-waveform numerical synthetics. *Tectonophysics*, 712-71. pp. 736-746. ISSN: 0040-1951

<https://doi.org/10.1016/j.tecto.2017.06.034>

(c) 2017 Published by Elsevier B.V. This manuscript version is made available under the CC BY-NC-ND 4.0 license <http://creativecommons.org/licenses/by-nc-nd/4.0/>

Reuse

Items deposited in White Rose Research Online are protected by copyright, with all rights reserved unless indicated otherwise. They may be downloaded and/or printed for private study, or other acts as permitted by national copyright laws. The publisher or other rights holders may allow further reproduction and re-use of the full text version. This is indicated by the licence information on the White Rose Research Online record for the item.

Takedown

If you consider content in White Rose Research Online to be in breach of UK law, please notify us by emailing eprints@whiterose.ac.uk including the URL of the record and the reason for the withdrawal request.

1 Fracture parameter inversion from passive seismic
2 shear-wave splitting: A validation study using
3 full-waveform numerical synthetics

4 Yousef¹, B.M., Almarzooq¹, H., Angus², D.A. & Hildyard¹, M.W.

5 1. School of Earth & Environment, University of Leeds, Leeds, UK

6 2. ESG Solutions, Kingston, Canada

7 **Abstract**

8 Fractures are pervasive features within the Earth's crust and they have a signif-
9 icant influence on the multi-physical response of the subsurface. The presence
10 of coherent fracture sets often leads to observable seismic anisotropy enabling
11 seismic techniques to remotely locate and characterise fracture systems. Since
12 fractures play a critical role in the geomechanical and fluid-flow response, there
13 has been significant interest in quantitatively imaging in situ fractures for im-
14 proved hydro-mechanical modelling. In this study we assess the robustness of
15 inverting for fracture properties using shear-wave splitting measurements. We
16 show that it is feasible to invert shear-wave splitting measurements to quan-
17 titatively estimate fracture strike and fracture density assuming an effective
18 medium fracture model. Although the SWS results themselves are diagnostic of
19 fracturing, the fracture inversion allows placing constraints on the physical prop-
20 erties of the fracture system. For the single seismic source case and optimum
21 receiver array geometry, the inversion for strike has average errors of between
22 11° and 25°, whereas for density has average errors between 65% and 80% for
23 the single fracture set and 30% and 90% for the double fracture sets. For real
24 microseismic datasets, the range in magnitude of microseismicity (i.e., frequency
25 content), spatial distribution and variable source mechanisms suggests that the
26 inversion of fracture properties from SWS measurements is feasible.

27 *Keywords:* explicit fractures, finite-difference, fracture inversion,

29 **1. Introduction**

30 Fractures are pervasive features within the brittle crust, ranging in size over
31 several orders of magnitude, from large scale faults (km) down to micro-cracks
32 in core samples (mm). Fractures play a critical role in the multi-physical re-
33 sponse of Earth materials, influencing the stress and strain fields leading to
34 geomechanical deformation as well as acting as secondary conduits for fluid-
35 flow contributing to fluid movement in porous media. Fractures also influence
36 the geophysical response of the subsurface, such as modifying seismic velocities
37 due to stress-dependent fracture stiffness.

38 Three-dimensional hydro-mechanical (HM) modelling of subsurface reser-
39 voirs has significantly progressed in the past decade to help the petroleum in-
40 dustry efficiently and safely extract hydrocarbons from unconventional reser-
41 voirs, such as shale-gas and coal-seam methane, and extreme environments at
42 high-pressures and temperatures. Furthermore, with the recent drive to reduce
43 anthropogenic CO₂ emissions using carbon capture and geo-sequestration, HM
44 modelling is a necessary step to predict risk and storage security. However, HM
45 models need to be calibrated using real physical measurements, such as pore
46 pressures, surface subsidence, and time-lapse and passive seismic monitoring.
47 Since fractures play a critical role in the geomechanical and fluid-flow response,
48 there has been significant interest in quantitatively imaging in situ fractures for
49 improved HM modelling.

50 The fact that fractures form coherent regions with directional dependence
51 of decreased stiffness leads to observable seismic anisotropy. Seismic anisotropy
52 refers to directional variations in seismic velocities, which in reservoirs is due to
53 intrinsic anisotropy, preferred alignment of sub-seismic scale fractures and the
54 influence of non-hydrostatic changes in the stress field on micro-cracks and grain
55 boundaries. There are several seismic methods that can be used to infer fracture
56 properties in the subsurface; the most common being anisotropic velocity model

57 analysis (e.g., Jones, 2010), amplitude versus offset and azimuth (AVOA) anal-
58 ysis (e.g., Liu & Martinez, 2012) and shear-wave splitting (SWS) analysis (e.g.,
59 Savage, 1999). These approaches can infer orientation and density of fractures
60 as well as monitor temporal and spatial variations in fracture properties (e.g.,
61 Teanby et al., 2004a).

62 Although azimuthal variation in velocity and reflection amplitude of P- and
63 S-waves can be diagnostic of anisotropy, shear-wave splitting (SWS) is the least
64 ambiguous indicator of seismic anisotropy. When a shear-wave from an isotropic
65 medium enters an anisotropic region it splits into two orthogonally polarised
66 waves, the S_1 -wave will travel faster than the S_2 -wave. The degree of split-
67 ting depends on the initial S-wave polarisation in the isotropic medium and
68 the allowable polarisation defined by the anisotropic elasticity tensor (e.g., An-
69 gus et al., 2004). SWS measures the polarisation direction (ϕ) of the fast S_1 -
70 wave and the delay time (δt) between the S_1 - and the S_2 - waves (e.g., Shearer,
71 2009). This delay time is proportional to the length of the ray path inside the
72 anisotropic medium and the strength of the seismic anisotropy (e.g., Wuestefeld
73 et al., 2011a). The delay time δt is normalised by the path length between
74 the source and the receiver to yield a percentage difference in S-wave velocity
75 δV_S . There have been several studies that have used SWS results to infer (e.g.,
76 Teanby et al., 2004b; Al-Harrasi et al., 2011; Yousef & Angus, 2016) or invert
77 (e.g., Verdon et al., 2009, 2011; Verdon & Wüstefeld, 2013) for various fracture
78 properties, such as fracture density and fracture orientation. SWS inversion
79 techniques use sets of delay times and fast polarisations along with source-to-
80 receiver information such as raypath azimuth, inclination, and travel distance
81 (e.g., Verdon et al., 2009; Wookey, 2012) to image fracture zones and estimate
82 in situ fracture properties.

83 A significant aspect of the subsurface multi-physical response relates the
84 stiffness of discrete fracture systems. The most common approach for modelling
85 the seismic and geomechanical behaviour of fractured rock is to use an effec-
86 tive medium model (EMM) representation of the fracture network. Although
87 EMM methods have been very useful, there are limitations such as the applica-

88 ble frequency range, the types of fracture properties which can be studied, and
89 non-uniform influences of, for example, the stress field. The discrete fracture
90 model (DFM) representation is an alternative approach to model fracture net-
91 works, where the fractures are considered as discrete or explicit discontinuities.
92 The DFM representation allows relaxing many of the required EMM assump-
93 tions and enables the solution to simulate the interaction of seismic waves with
94 fractures systems more accurately, such as modelling the influence of stress state
95 as well as fracture size, fill and stiffness.

96 In this paper, we study the feasibility of inverting for fracture strike (α)
97 and density (ϵ) for several fracture models having one set of fractures or two
98 sets of orthogonally aligned fractures using microseismic SWS measurements.
99 To do this, we generate a suite of 96 fracture models each for the single and
100 double fracture set geometries with varying fracture size, density, stiffness and
101 effective compliance ratio (we introduce compliance ratio rather than stiffness
102 ratio because it is pervasive in the fracture-induced seismic anisotropy litera-
103 ture). For each model, we generate full-waveform microseismic synthetics using
104 the 3D finite-difference (FD) algorithm WAVE (Hildyard, 2007). The seismic
105 anisotropy induced by the fractures is measured using SWS delay times and fast
106 polarisation directions utilising the approach of Teanby et al. (2004a). Based on
107 an effective medium fracture model, the SWS measurements are inverted for the
108 best fitting fracture model parameters (α and ϵ) using the approach of Verdon
109 & Wüstefeld (2013) and Verdon et al. (2011, 2009). We subsequently compare
110 the inversion results to the true model to evaluate the feasibility of the inversion
111 approach in extracting fracture properties from SWS data.

112 **2. Model**

113 We simulate wave propagation through a suite of elastic models: one subset
114 of models having a single set of aligned fractures and another subset having
115 two orthogonally aligned fracture sets within a homogeneous isotropic medium
116 (Yousef & Angus, 2016, 2017). The background model is isotropic with P-wave

117 velocity of 5700 m/s, S-wave velocity of 3200 m/s and density of 2600 kg/m³.
 118 For each model, a total of 69 3C receivers are used (see Figure 1), with 20
 119 receivers placed in vertical boreholes (four boreholes each containing 5 receivers)
 120 and the remaining 49 receivers forming a planar near-surface square array (the
 121 near surface array is buried to eliminate free surface noise contamination). The
 122 dimension of the elastic model is 300 m × 300 m × 300 m. A microseismic source
 123 is defined having a Ricker wavelet with dominant frequency of approximation
 124 180 Hz. The source mechanism is a moment tensor having a seismic moment
 125 magnitude of 1×10^{14} dyne cm and a strike-slip double-couple mechanism with
 126 strike 90°, dip of 90° and slip 45°. To reduce the computational time and
 127 allow exploring the influence of fracture properties on the fracture inversion, we
 128 simulate one event for each fracture model. In practice, numerous microseismic
 129 events would be recorded during microseismic monitoring and so many source-
 130 receiver SWS measurements would be used to invert for fracture properties.
 131 However, the synthetic data are noise free and so allow studying the feasibility
 132 of inverting microseismic SWS for fracture properties.

133 A total of 96 models have been generated: varying the fracture size a ($a= 6$,
 134 10, 20 and 50 m), fracture density ϵ ($\epsilon= 0.02, 0.04, 0.08$ and 0.1) and fracture
 135 compliance ratio Z_N/Z_T ($Z_N/Z_T= 0.33, 0.60$ and 1.00) (see Table 1). In this
 136 study, fracture density is defined (Hildyard, 2007)

$$\epsilon = \frac{1}{2\pi V} \sum a^3, \quad (1)$$

137 where V is volume encompassing the fractures, summation is over all discrete
 138 fractures within V and the fractures are assumed to be square cracks. The
 139 fracture stiffness values are divided into high stiffness models (HS) and low
 140 stiffness model (LS). The LS models have values of (1, 5 and 6) × 10¹⁰ Pa/m
 141 for the normal fracture stiffness K_N and (1, 3 and 2) × 10¹⁰ Pa/m for the shear
 142 fracture stiffness K_S . Similar values for the HS models have been chosen with
 143 the exception that these models have higher stiffness by one order of magnitude.
 144 These values were chosen based on the ranges of values observed in the field

145 and laboratory (e.g., Lubbe & Worthington, 2006; Verdon & Wüstefeld, 2013).
146 For the orthogonal double fracture sets, fracture properties are kept identical
147 between the fracture sets to simplify the modelling procedure.

148 **3. SWS results**

149 For all 96 models, a total of 6624 3C seismograms have been processed,
150 where we pick the P- and S-wave arrivals, rotate the 3C seismograms from
151 the global coordinate system (i.e., east, north and vertical) into the local ray
152 (source-receiver) coordinate system (i.e., the ray or P-wave direction and the S_V
153 and S_H directions), and filtered the waveforms using a Butterworth bandpass
154 filter between 10 Hz and 1500 Hz, which is the range of the expected frequencies.
155 After rotation, we calculate the SWS delay time δt and fast polarisation direction
156 (ϕ). After parameter and quality control tests, a P-wave window size of 0.02
157 s is chosen, where we allow the S-wave window size to vary slightly around
158 0.01 s (the maximum δt value is constrained to be 3 ms). Next, SWS analysis
159 is performed for each 3C seismogram. For each measurement, a diagnostic
160 plot is created and is used to determine whether a SWS result is good, null
161 or bad. A SWS measurement is classified using an automated quality control
162 value (\mathbb{Q}) and is a measure of how similar the SWS measurement parameters of
163 the cross-correlation (XC) and eigenvalue (EV) techniques are (see Wuestefeld
164 et al., 2010, for details). In addition to the automated quality control measure,
165 the SWS measurements can be assessed using the diagnostic plots from the EV
166 method. A SWS measurement is considered reliable by determining whether (1)
167 the energy on the corrected transverse component has been minimised, (2) the
168 S_1 - and S_2 -waves have similar waveforms, and (3) the elliptical S-wave particle
169 motion in the SV-SH plane has been linearised after the splitting correction.
170 The value of \mathbb{Q} ranges from -1 to +1, where $\mathbb{Q} = -1$ denotes a null result (i.e.,
171 no anisotropy and hence no SWS), $\mathbb{Q} = 0$ denoting a poor result (i.e., unreliable)
172 and $\mathbb{Q} = +1$ denoting a good result (i.e., SWS present). We define a \mathbb{Q} value
173 of greater than or equal to 0.75 to be a good SWS result for the synthetic

174 seismograms based on trial and error (i.e., $\mathbb{Q} < 0.75$ resulted in inaccurate
175 fracture inversions). Figure 2 shows an example of a SWS diagnostic plot with
176 a good quality factor ($\mathbb{Q} = 0.96$) and an example of the null result ($\mathbb{Q} = -0.98$).
177 For the good quality factor (Figure 2a) the particle motion is ellipsoidal before
178 correction and is linearised after correction while for the null SWS (Figure 2b)
179 the particle motion is linear before and after the correction.

180 3.1. Single fracture set vs double fracture sets

181 For the models having one fracture set, the fracture strike is $\alpha=90^\circ$ from
182 north (i.e., the Y-axis), whereas for the double fracture set models the fracture
183 sets have strike $\alpha= 0^\circ$ and 90° (i.e., the fractures are orthogonal along the X-
184 and Y-axes). Figure 3 depicts the ray coverage in the vertical (inclination) and
185 horizontal (azimuth) planes. There is good azimuth coverage with the exception
186 of a reduction in azimuthal coverage between 210° and 300° . The range of
187 inclination covers mainly between 0° and 60° with some coverage between 60°
188 and 110° . Out of 6624 source-receiver combination there are 445 good SWS
189 measurements ($\approx 7\%$) for the single fracture set models, where as for the double
190 fracture set models there are 261 good SWS measurements ($\approx 4\%$). This is likely
191 due to the presence of the additional fracture set which reduces the amount of
192 coherent scattering that allows SWS to develop (Yousef & Angus, 2016).

193 Figure 4 is a histogram for azimuth and inclination of the good SWS mea-
194 surements for the both single and double fracture set models. The figure shows
195 that the majority of the raypaths are between 40° and 120° azimuth travel sub-
196 horizontally through the fracture volume. There is no azimuth coverage between
197 0° and 40° as well as 140° and 180° since the raypaths do not travel through
198 the fracture volume where SWS would develop. The highest azimuthal counts
199 in the histogram are for the vertical borehole arrays.

200 Figure 5 shows the distribution of \mathbb{Q} against the difference between initial
201 S-wave polarisation and ϕ in the shear-wave plane (i.e., SV-SH plane). The null
202 measurements can be seen clearly in this figure. Good quality SWS measure-
203 ments require a separation of at least 20° from the null direction. The scatter

204 reveals that higher Q values occur when the difference is approximately 45° ,
 205 and lower Q values when differences equal to 0° and 90° . This figure confirms
 206 the automated quality control approach has a physical basis. However, it would
 207 be expected that the signal-to-noise ratio can influence this approach (Wueste-
 208 feld et al., 2010). It can be seen for the whole dataset that most of the SWS
 209 measurements fall in the category of good null ($Q < -0.75$). The key point to
 210 make is that the SWS quality measure allows for a reduction in the required
 211 visual examination of the diagnostic plots (Al-Harrasi et al., 2011). Since the
 212 dataset is noise free and the model geometry is designed to maximise S-wave
 213 anisotropy, we can automatically control and choose the high SWS measure-
 214 ment quality reliably from the large volume of data. Similarly, Wuestefeld et al.
 215 (2010) applied this approach to a Valhall microseismic dataset with the results
 216 of the automated SWS analysis being equivalent with the manual results of
 217 Teanby et al. (2004b).

218 To make the SWS less subjective, the Q value is introduced and is calculated
 219 from the combination of both the EV and XC techniques. Both techniques
 220 behave differently, particularly in the vicinity of the null direction, where the XC
 221 technique fails to extract proper values of ϕ_{XC} and δt_{XC} . This occurs because
 222 of the absence or the weakness of S-wave energy on the transverse component
 223 close to the null. In fact, correlation can only be found if the rotations of the grid
 224 search transfer energy from the initial polarization component to the transverse
 225 component. The correlation is maximum for a rotation of 45° and obviously
 226 results in zero time lag between the two S-wave components. Therefore, the
 227 techniques should not be used alone (Wustefeld & Bokelmann, 2007). The
 228 Q value is crucial for reliable fracture inversion of anisotropy measurements;
 229 the results of the inversion are dependent on the Q values of the input SWS
 230 measurements.

231 The number of good SWS measurements is a key parameter in the inversion
 232 for fracture properties. Based on trial and error and considering the stability of
 233 the inversion results for each model, we perform the fracture inversion with a
 234 minimum of 5 SWS measurements with $Q \geq 0.75$, generally leading to a stable

235 inversion. Figure 6 plots the histograms of δt for the whole dataset and good
 236 SWS data for both single and double fracture sets. For the whole dataset δt is
 237 approximately flat between 0 to 3 ms with higher number of SWS measurements
 238 at 0 ms and 3 ms. In contrast, for the good SWS measurements, the δt values
 239 the double fracture set models are roughly flat between 0.25 to 2.75 ms and for
 240 the single fracture set is similar but with a skewed distribution centred towards
 241 lower δt values.

242 In Figure 7, we plot the published compliance (i.e., inverse stiffness) values
 243 versus fracture size a (grey rectangles) from literature (Lubbe, 2005; Pyrak-
 244 Nolte et al., 1990; Hardin et al., 1987; Lubbe & Worthington, 2006; King et al.,
 245 1986; Worthington & Hudson, 2000) as well as the model values (see table 1)
 246 generated in this study. For the three compliance ratios $Z_N/Z_T = 0.33, 0.60$
 247 and 1.00 and fracture sizes $a = 6, 10, 20$ and 50 m the results are categorised into
 248 good, unstable and no SWS. The models with good SWS are those that have 5
 249 or more good SWS values $\mathbb{Q} \geq 0.75$ (red), the models with unstable SWS have
 250 less than 5 good SWS values (blue) and the models with no SWS (black). The
 251 dashed diagonal line in Figure 7 represents the inferred scale dependence of the
 252 normal or shear fracture compliance (or stiffness) with fracture size. From Fig-
 253 ure 7, it can be observed that by increasing the fracture density ϵ the number of
 254 models with good SWS increases, particularly for small fractures. Furthermore,
 255 by increasing the compliance Z_N and Z_T (or decreasing stiffness) by one order
 256 of magnitude while keeping Z_N/Z_T constant leads to models with good SWS,
 257 except for models with fracture size $a = 50$ m and $Z_N/Z_T \geq 0.60$. However, the
 258 poor SWS results are due to the fewer number of fractures (i.e., the maximum
 259 number is 3) the wave interacts with between source and receivers.

260

261

262 **4. EMM inversion method**

263 In this section, the EMM inversion algorithm of (Verdon et al., 2009) is used
 264 to invert for fracture strike α and fracture density ϵ . A primary motivation
 265 for this study was to assess the key assumption of the inversion approach of
 266 Verdon et al. (2009), that the whole path length between source and receiver is
 267 fully anisotropic. From a geological perspective, this is unlikely to be a valid as-
 268 sumption. Although minerals are typically anisotropic and that it is recognized
 269 that sedimentary layering and fracture systems can induce seismic anisotropy,
 270 there must be a coherent fabric over several length scales with respect to the
 271 probing seismic wavefield such that anisotropy can develop (e.g., Yousef & An-
 272 gus, 2016). The measured SWS parameters ϕ and δt are influenced by the path
 273 length within an anisotropic volume only, yet directly relating the SWS param-
 274 eters to the medium elasticity (e.g., strength of anisotropy) requires knowledge
 275 of either the fast and slow shear-wave velocity or the path length within the
 276 anisotropic volume. In other words, although δt can be used to characterise the
 277 strength of anisotropy, there is a trade off in terms of the distance travelled in
 278 the anisotropic volume and the strength of the seismic anisotropy. Thus the
 279 δt parameter is typically normalised by an assumed path length D to estimate
 280 the percentage velocity anisotropy δV_S (i.e., difference between S_1 and S_2 ve-
 281 locity). The δV_S parameter can be computed using the following relationship
 282 (e.g., Baird et al., 2013):

$$\delta V_S = 100 \frac{V_{S1} - V_{S2}}{(V_{S1} + V_{S2})/2}, \quad (2)$$

283 where t is the traveltime and $V_{S1} = D/t$ is velocity of the fast S-wave, and $V_{S2} =$
 284 $D/(t + \delta t)$ is the velocity of the slow S-wave. For the results in this study and
 285 assuming the full raypath is within an anisotropic volume, the maximum S-wave
 286 velocity anisotropy δV_S for the single and double fracture sets are approximately
 287 16% and 21%, respectively.

288 To obtain reliable inversion results, the inversion is performed for models
 289 with at least 5 good SWS results ($Q \geq 0.75$). To assess the inversion approach,

290 we first invert for the fracture properties of the single vertical fracture set mod-
 291 els, which represent a simpler model and hence, in principle, a more constrained
 292 inversion. Subsequently, we then invert for fracture properties of the orthogonal
 293 fracture set models (orthorhombic model). The algorithm allows for the inver-
 294 sion for background VTI anisotropy (e.g., Verdon et al., 2011), but since the
 295 background medium is isotropic the anisotropy parameters are excluded from
 296 the inversion process. Therefore, the independent parameters in the inversion
 297 are fracture strike and fracture density for the single and double fracture set
 298 models.

299 We should note that the EMM inversion uses an effective fracture compliance
 300 (B_N , B_T with unit Pa^{-1}) as a representation of the whole discrete fracture
 301 volume rather than individual fracture compliance (Z_N , Z_T with unit m Pa^{-1}).
 302 Unlike B_N and B_T , that describe the equivalent medium compliance of a full
 303 fracture set and have dimension $1/\text{stress}$ (Pa^{-1}), Z_N and Z_T are compliances
 304 of the individual discrete fracture with dimension length/stress (m/Pa). The
 305 $Z_{(N,T)}$ and $B_{(N,T)}$ can be related through the following equation

$$B_{(N,T)} = \frac{Z_{(N,T)}}{H}, \quad (3)$$

306 where H is the average fracture spacing in a direction normal to the fracture
 307 surface (Worthington, 2008).

308 In order to obtain the optimum estimates of fracture strike and fracture
 309 density and also minimise the computation time of the inversion, we limit the
 310 grid search to sensible values for these parameters. For the single fracture
 311 inversion, we allow α to vary between 0° and 180° , whereas for the double
 312 fracture inversion, we allow α_1 and α_2 to vary between $\alpha_1 = -45^\circ$ and 45°
 313 and $\alpha_2 = 45^\circ$ and 135° for the first and second fracture sets. Following the
 314 assumption of Crampin (1994) that fracture density is roughly equal to one
 315 hundredth of δV_S and assuming a maximum δV_S of 21%, we set the fracture
 316 density range to be between 0.00 and 0.14 for both the single and double fracture
 317 sets.

318 **5. Results**

319 *5.1. Single fracture set*

320 Figure 8 shows the inversion results for α and ϵ for the single fracture set
321 models as a polar plot diagram. The inverted fracture strikes fall within $\pm 40^\circ$ of
322 the true model fracture strike $\alpha = 90^\circ$. The inverted strikes for the $Z_N/Z_T =$
323 0.60 are more tightly constrained around the true model. The average and
324 standard deviation of the inversion results for the three categories of compliance
325 ratio Z_N/Z_T are given in Table 3. A general observation from the inversion
326 results of the single fracture models suggests that fracture strike is much better
327 constrained than fracture density, consistent with the results of Verdon et al.
328 (2011); Yousef & Angus (2016).

329 *5.2. Double fracture sets*

330 Figure 9 shows the inversion results for fracture strike (α_1 and α_2) and
331 fracture density (ϵ_1 and ϵ_2) for the double fracture set models. The results
332 reveal that the inverted fracture strike and density for fracture set 2 are better
333 constrained than those for fracture set 1. The inverted fracture strikes are close
334 to the true model fracture strikes (i.e., 0° and 90°), indicating that the inversion
335 for strike has been successful. However, the inverted fracture densities are less
336 accurate when the fracture sets are orthogonal. This finding is consistent with
337 the inverted fracture densities of Verdon et al. (2009). Furthermore, Grechka &
338 Tsvankin (2003) have discussed that it is possible for a broad range of fracture
339 density models to produce an equivalent effective medium stiffness tensor. Table
340 4 lists the average errors in the inversion for fracture strike and density for both
341 fracture sets for each compliance ratio Z_N/Z_T . Since the fractures in the model
342 are orthogonal, we examine the orthogonality of the inverted fracture strikes.
343 Figure 10 shows a polar plot diagram of the difference in strike between the
344 inverted fracture strikes $\Delta\alpha$. The plot reveals that the majority of the inversions
345 have $\Delta\alpha = 90^\circ \pm 30^\circ$. From Figure 10 it can be observed that the inversion
346 results for fracture densities versus $\Delta\alpha$ are better constrained with increasing
347 compliance ratio Z_N/Z_T .

348 Figure 11 presents the inverted fracture strike versus fracture density for
349 both single and double fracture set models. From this figure, it is apparent that
350 the maximum strike inversion error for the single fracture set models (i.e., 80°)
351 is approximately double of those results for the double fracture set. In contrast,
352 the inversion error for fracture density for both single and double fracture set
353 models are generally between 40% and 100%.

354 6. Discussion

355 From Figures 8 to 9 it can be observed that the inversion algorithm is capable
356 of estimating fracture strike without prior knowledge of the medium fracture
357 properties. The outliers are likely influenced by the non-linear nature of the
358 inversion algorithm and the fact that the inversion uses only a single event to
359 characterise a finite fracture volume. Furthermore, the location of the source
360 and orientation of failure source mechanism may be insufficient to illuminate
361 the fracture set. However, with more sources spatially distributed around the
362 fracture volume and more favourable (i.e, more data) it is possible that the
363 fracture inversion would yield more accurate results (Rial et al., 2005). For the
364 double fracture set models, the inverted strike for the 0° fracture set degrades,
365 whereas the inverted strike for the 90° fracture set appears to be better resolved
366 (broader but fewer outliers). Improvements on resolving strike can be made by
367 including more microseismic sources in the inversion process.

368 In contrast, it should be noted that the inverted fracture densities are sys-
369 tematically underestimated from the true value for the single fracture set (i.e.,
370 the inversion results clustered between 0.00 and 0.06), while it is systematically
371 overestimated for the double fracture sets for the low compliance ratios (i.e.,
372 $Z_N/Z_T = 0.33$ and 0.60). This seems to be mainly caused by the both fracture
373 densities in the real model being constant and secondly, a trade-off between the
374 two fracture densities that is inherent in the inversion as noted by Verdon et al.
375 (2011). More importantly, the EMM inversion algorithm assumes that the whole
376 medium in which the ray traverses is fractured, instead of only a portion of the

377 raypath within fracture zone. This is likely the main cause of the poor estimates
378 of fracture density. Improvements in resolving fracture density (or stiffness) can
379 be achieved using a more advanced inversion approach such as anisotropic to-
380 mography in which the medium can be divided into different domains with each
381 domain having different anisotropic characteristics (e.g., Abt & Fischer, 2008;
382 Wookey, 2012). However, Yousef & Angus (2016) show that the inaccurate es-
383 timates of fracture density is influenced also by the choice of effective medium
384 rock physics model. For this study, the inadequacy of the linear-slip model is
385 a contributing factor in the poor estimates of fracture density (e.g., Yousef &
386 Angus, 2016).

387 **7. Conclusions**

388 We have shown that it is feasible to invert SWS measurements to quantita-
389 tively estimate fracture strike and fracture density assuming an effective medium
390 fracture model. The results of the full waveform FD synthetics indicate that
391 the source frequency of the microseismicity will be crucial in extracting reli-
392 able fracture parameters due to the relationship between scale length of the
393 probing seismic wave and the fracture heterogeneity (i.e., size). Although the
394 SWS results themselves are diagnostic of fracturing, the fracture inversion al-
395 lows placing constraints on the physical properties of the fracture system. For
396 real microseismic datasets, the range in magnitude of microseismicity (i.e., fre-
397 quency content), spatial distribution and variable source mechanisms suggests
398 that the inversion of fracture properties from SWS measurements is feasible.
399 For the single seismic source case and optimum receiver array geometry, the in-
400 version for strike has average errors of between 11° and 25° , whereas for density
401 has average errors between 65% and 80% for the single fracture set and 30%
402 and 90% for the double fracture sets.

403 **Acknowledgments**

404 B. Yousef would like to acknowledge Kurdistan regional government for their
405 financial support of his PhD study. D. Angus acknowledges the Research Coun-
406 cil UK (EP/K035878/1; EP/K021869/1; NE/L000423/1) and M. Hildyard ac-
407 knowledges the Research Council UK (NE/L000423/1) for financial support.

408 **References**

- 409 Abt, D. L., & Fischer, K. M. (2008). Resolving three-dimensional anisotropic
410 structure with shear wave splitting tomography. *Geophysical Journal Inter-*
411 *national*, *173*, 859–886.
- 412 Al-Harrasi, O., Al-Anboori, A., Wüstefeld, A., & Kendall, J. M. (2011). Seismic
413 anisotropy in a hydrocarbon field estimated from microseismic data. *Geophys-*
414 *ical Prospecting*, *59*, 227–243.
- 415 Angus, D. A., Thomson, C. J., & Pratt, R. G. (2004). A one-way wave equa-
416 tion for modelling variations in seismic waveforms due to elastic anisotropy.
417 *Geophysical Journal International*, *156*, 595–614.
- 418 Baird, A. F., Kendall, J.-M., & Angus, D. A. (2013). Frequency-dependent
419 seismic anisotropy due to fractures: Fluid flow versus scattering. *Geophysics*,
420 *78*, WA111–WA122.
- 421 Crampin, S. (1994). The fracture criticality of crustal rocks. *Geophysical Journal*
422 *International*, *118*, 428–438.
- 423 Grechka, V., & Tsvankin, I. (2003). Feasibility of seismic characterization of
424 multiple fracture sets. *Geophysics*, *68*, 1399–1407.
- 425 Hardin, E., Cheng, C., Paillet, F., & Mendelson, J. (1987). Fracture charac-
426 terization by means of attenuation and generation of tube waves in fractured
427 crystalline rock at mirror lake, new hampshire. *Journal of Geophysical Re-*
428 *search: Solid Earth (1978–2012)*, *92*, 7989–8006.

- 429 Hildyard, M. (2007). Manuel rocha medal recipient wave interaction with un-
430 derground openings in fractured rock. *Rock Mechanics and Rock Engineering*,
431 *40*, 531–561.
- 432 Jones, I. F. (2010). *An Introduction to Velocity Model Building*. EAGE.
- 433 King, M. S., Myer, L. R., & Rezowalli, J. J. (1986). Experimental studies
434 of elastic-wave propagation in a columnar-jointed rock mass. *Geophysical*
435 *Prospecting*, *34*, 1185–1199.
- 436 Liu, E., & Martinez, A. (2012). Seismic fracture characterization: Concepts and
437 practical applications, . (p. 280).
- 438 Lubbe, R. (2005). A field and laboratory investigation of the compliance of
439 fractured rock. *DPhil thesis, Oxford University*.
- 440 Lubbe, R., & Worthington, M. H. (2006). A field investigation of fracture
441 compliance. *Geophysical Prospecting*, *54*, 319–331.
- 442 Pyrak-Nolte, L. J., Myer, L. R., & Cook, N. G. W. (1990). Anisotropy in
443 seismic velocities and amplitudes from multiple parallel fractures. *Journal of*
444 *Geophysical Research-Solid Earth and Planets*, *95*, 11345–11358.
- 445 Rial, J. A., Elkibbi, M., & Yang, M. (2005). Shear-wave splitting as a tool
446 for the characterization of geothermal fractured reservoirs: lessons learned.
447 *Geothermics*, *34*, 365–385.
- 448 Savage, M. (1999). Seismic anisotropy and mantle deformation: What have we
449 learned from shear wave splitting? *Reviews Of Geophysics*, *37*, 65–106.
- 450 Shearer, P. M. (2009). *Introduction to seismology*. Cambridge University Press.
- 451 Teanby, N., Kendall, J.-M., & Van der Baan, M. (2004a). Automation of shear-
452 wave splitting measurements using cluster analysis. *Bulletin of the Seismo-*
453 *logical Society of America*, *94*, 453–463.

- 454 Teanby, N., Kendall, J.-M., Jones, R., & Barkved, O. (2004b). Stress-induced
455 temporal variations in seismic anisotropy observed in microseismic data. *Geo-*
456 *physical Journal International*, *156*, 459–466.
- 457 Verdon, J., Kendall, J.-M., & Wüstefeld, A. (2009). Imaging fractures and
458 sedimentary fabrics using shear wave splitting measurements made on passive
459 seismic data. *Geophysical Journal International*, *179*, 1245–1254.
- 460 Verdon, J. P., Kendall, J. et al. (2011). Detection of multiple fracture sets
461 using observations of shear-wave splitting in microseismic data. *Geophysical*
462 *Prospecting*, *59*, 593–608.
- 463 Verdon, J. P., & Wüstefeld, A. (2013). Measurement of the normal/tangential
464 fracture compliance ratio (z_n/z_t) during hydraulic fracture stimulation using
465 s-wave splitting data. *Geophysical Prospecting*, *61*, 461–475.
- 466 Wookey, J. (2012). Direct probabilistic inversion of shear wave data for seismic
467 anisotropy. *Geophysical Journal International*, *189*, 1025–1037.
- 468 Worthington, M. (2008). Interpreting seismic anisotropy in fractured reservoirs.
469 *First Break*, *26*.
- 470 Worthington, M., & Hudson, J. (2000). Fault properties from seismic q. *Geo-*
471 *physical Journal International*, *143*, 937–944.
- 472 Wuestefeld, A., Al-Harrasi, O., Verdon, J. P., Wookey, J., & Kendall, J. M.
473 (2010). A strategy for automated analysis of passive microseismic data to im-
474 age seismic anisotropy and fracture characteristics. *Geophysical Prospecting*,
475 *58*, 755–773.
- 476 Wuestefeld, A., Verdon, J. P., Kendall, J.-M., Rutledge, J., Clarke, H., &
477 Wookey, J. (2011a). Inferring rock fracture evolution during reservoir stimu-
478 lation from seismic anisotropy. *Geophysics*, *76*, WC157–WC166.
- 479 Wustefeld, A., & Bokelmann, G. (2007). Null detection in shear-wave splitting
480 measurements. *Bulletin of the Seismological Society of America*, *97*, 1204–
481 1211.

- 482 Yousef, B. M., & Angus, D. A. (2016). When do fractured media become
483 seismically anisotropic? some implications on quantifying fracture properties.
484 *Earth and Planetary Science Letters*, *444*, 150–159.
- 485 Yousef, B. M., & Angus, D. A. (2017). Analysis of fracture induced scattering
486 of microseismic shear-waves. *Studia Geophysica et Geodaetica*, *61*, 26.

$Z_N/Z_T = 0.33$								
Fracture density	0.02		0.04		0.08		0.1	
size (m)	K_N	K_T	K_N	K_T	K_N	K_T	K_N	K_T
6	6×10^{10}	2×10^{10}	6×10^{10}	2×10^{10}	6×10^{10}	2×10^{10}	6×10^{10}	2×10^{10}
6	6×10^{11}	2×10^{11}	6×10^{11}	2×10^{11}	6×10^{11}	2×10^{11}	6×10^{11}	2×10^{11}
10	3×10^{10}	1×10^{10}	3×10^{10}	1×10^{10}	3×10^{10}	1×10^{10}	3×10^{10}	1×10^{10}
10	3×10^{11}	1×10^{11}	3×10^{11}	1×10^{11}	3×10^{11}	1×10^{11}	3×10^{11}	1×10^{11}
20	3×10^9	1×10^9	3×10^9	1×10^9	3×10^9	1×10^9	3×10^9	1×10^9
20	3×10^{10}	1×10^{10}	3×10^{10}	1×10^{10}	3×10^{10}	1×10^{10}	3×10^{10}	1×10^{10}
50	3×10^9	1×10^9	3×10^9	1×10^9	3×10^9	1×10^9	3×10^9	1×10^9
50	3×10^{10}	1×10^{10}	3×10^{10}	1×10^{10}	3×10^{10}	1×10^{10}	3×10^{10}	1×10^{10}
$Z_N/Z_T = 0.6$								
Fracture density	0.02		0.04		0.08		0.1	
size (m)	K_N	K_T	K_N	K_T	K_N	K_T	K_N	K_T
6	5×10^{10}	3×10^{10}	5×10^{10}	3×10^{10}	5×10^{10}	3×10^{10}	5×10^{10}	3×10^{10}
6	5×10^{11}	3×10^{11}	5×10^{11}	3×10^{11}	5×10^{11}	3×10^{11}	5×10^{11}	3×10^{11}
10	5×10^{10}	3×10^{10}	5×10^{10}	3×10^{10}	5×10^{10}	3×10^{10}	5×10^{10}	3×10^{10}
10	5×10^{11}	3×10^{11}	5×10^{11}	3×10^{11}	5×10^{11}	3×10^{11}	5×10^{11}	3×10^{11}
20	5×10^9	3×10^9	5×10^9	3×10^9	5×10^9	3×10^9	5×10^9	3×10^9
20	5×10^{10}	3×10^{10}	5×10^{10}	3×10^{10}	5×10^{10}	3×10^{10}	5×10^{10}	3×10^{10}
50	5×10^9	3×10^9	5×10^9	3×10^9	5×10^9	3×10^9	5×10^9	3×10^9
50	5×10^{10}	3×10^{10}	5×10^{10}	3×10^{10}	5×10^{10}	3×10^{10}	5×10^{10}	3×10^{10}
$Z_N/Z_T = 1.0$								
Fracture density	0.02		0.04		0.08		0.1	
size (m)	K_N	K_T	K_N	K_T	K_N	K_T	K_N	K_T
6	1×10^{10}	1×10^{10}	1×10^{10}	1×10^{10}	1×10^{10}	1×10^{10}	1×10^{10}	1×10^{10}
6	1×10^{11}	1×10^{11}	1×10^{11}	1×10^{11}	1×10^{11}	1×10^{11}	1×10^{11}	1×10^{11}
10	3×10^{10}	3×10^{10}	3×10^{10}	3×10^{10}	3×10^{10}	3×10^{10}	3×10^{10}	3×10^{10}
10	3×10^{11}	3×10^{11}	3×10^{11}	3×10^{11}	3×10^{11}	3×10^{11}	3×10^{11}	3×10^{11}
20	1×10^9	1×10^9	1×10^9	1×10^9	1×10^9	1×10^9	1×10^9	1×10^9
20	1×10^{10}	1×10^{10}	1×10^{10}	1×10^{10}	1×10^{10}	1×10^{10}	1×10^{10}	1×10^{10}
50	3×10^9	3×10^9	3×10^9	3×10^9	3×10^9	3×10^9	3×10^9	3×10^9
50	3×10^{10}	3×10^{10}	3×10^{10}	3×10^{10}	3×10^{10}	3×10^{10}	3×10^{10}	3×10^{10}

Table 1: Summary of fracture properties for all models, where K_N and K_T are in units Pa/m .

Z_N/Z_T	0.33	0.6	1.0
$\Delta\epsilon$	70 ± 23	66.55 ± 27.52	68.69 ± 15.59
$\Delta\alpha$	23.02 ± 16.82	14 ± 17.24	10.57 ± 8.92

Table 2: Average fracture and density inversion error for the single fracture set models.

Z_N/Z_T	$\Delta\epsilon(\%)$	$\Delta\alpha(^{\circ})$
0.33	76.85 ± 41.62	24.00 ± 21.53
0.6	66.56 ± 25.74	16.19 ± 23.95
1.0	67.79 ± 16.36	11.40 ± 8.75

Table 3: Average error in fracture strike and density for the single fracture set models (given as average error \pm standard deviation).

Z_N/Z_T	$\Delta\epsilon 1(\%)$	$\Delta\alpha 1(^{\circ})$	$\Delta\epsilon 2(\%)$	$\Delta\alpha 2(^{\circ})$
0.33	88.38 ± 101.62	23.41 ± 13.73	60.21 ± 61.95	22.68 ± 11.97
0.6	67.61 ± 76.84	14.68 ± 9.78	31.64 ± 38.04	15.88 ± 12.39
1.0	40.83 ± 11.24	21.37 ± 16.93	60.08 ± 4.57	21.39 ± 15.15

Table 4: Average error in fracture strike and density error for the double fracture set models (given as average error \pm standard deviation).

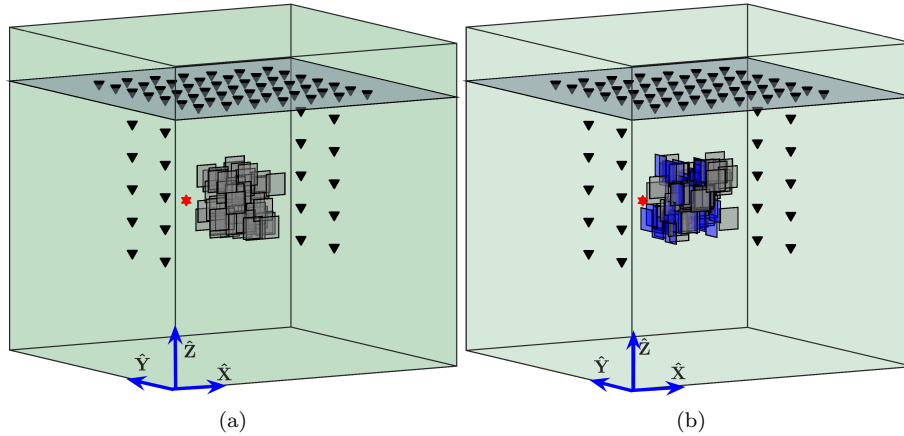
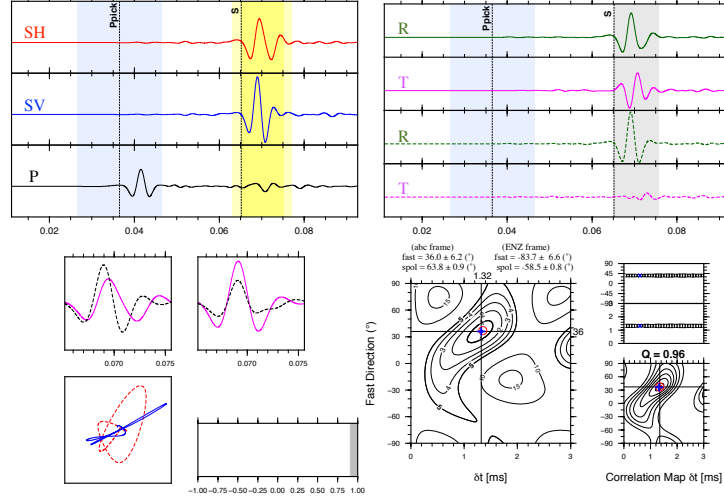
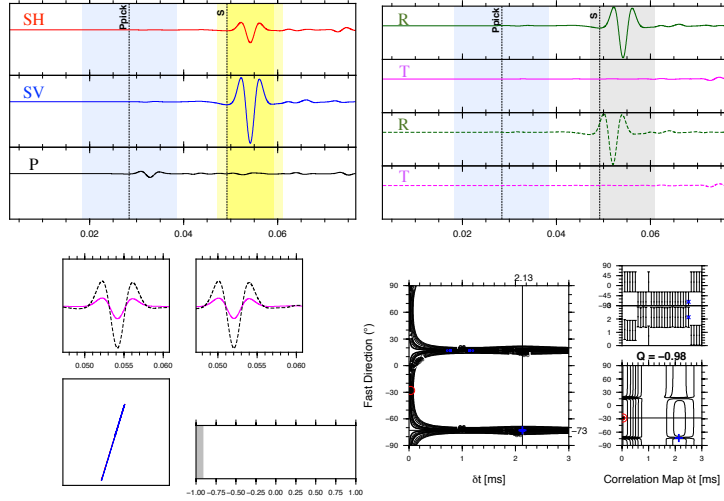


Figure 1: Geometry of the 3D FD model with (a) one set of aligned fractures and (b) two sets of aligned fractures. The red star represents the location of the micro-seismic source (located in the centre of the left edge of the fracture zone), the triangles represent the surface and borehole receivers and the grey and blue rectangles within the sub-volume schematically represent the vertical fractures.



(a)



(b)

Figure 2: Example of (a) good SWS measurement ($Q = 0.96$) and (b) null splitting ($Q = -0.98$). For (a) and (b); (top-left) 3 component waveforms in local ray coordinates; (top-right) radial and transverse components before (top 2 traces) and after (bottom 2 traces) splitting correction; (middle-left) fast (dashed) and slow (solid) S waves before (left) and after (right) correction; (bottom-left) particle motion in $SV-SH$ coordinate frame before (dashed) and after (solid) correction; (bottom-right) error surfaces of the eigenvalue (left) and cross-correlation (lower right) methods (see Wuestefeld et al., 2010, for details). The best result of the two methods are shown as blue + and red circle for the eigenvalue and cross-correlation method, respectively; and (middle-right) fast axis (top) and δt variations for each window including corresponding error bars.

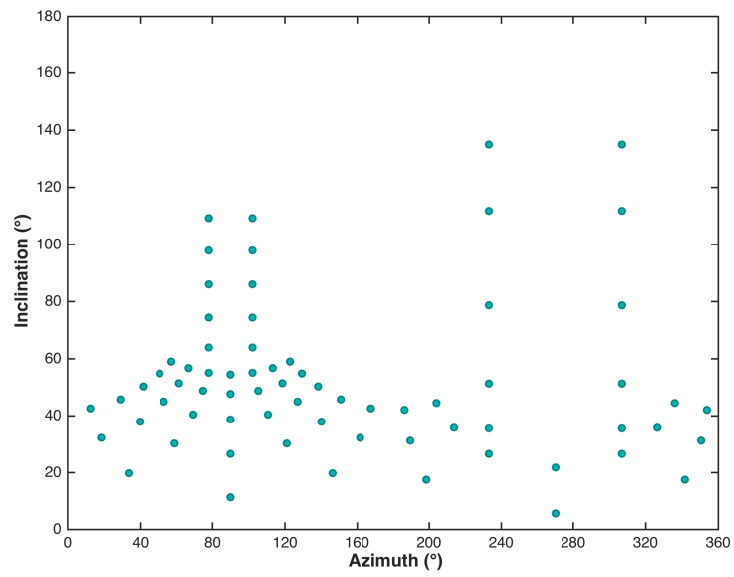


Figure 3: Distribution of source-receiver azimuth and inclination for the fracture model array.

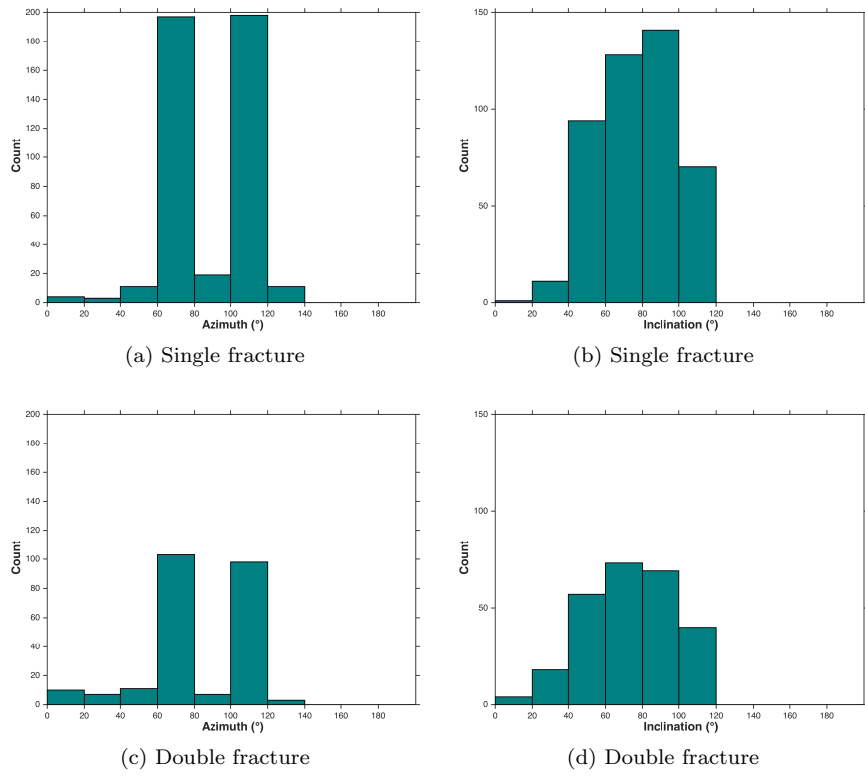
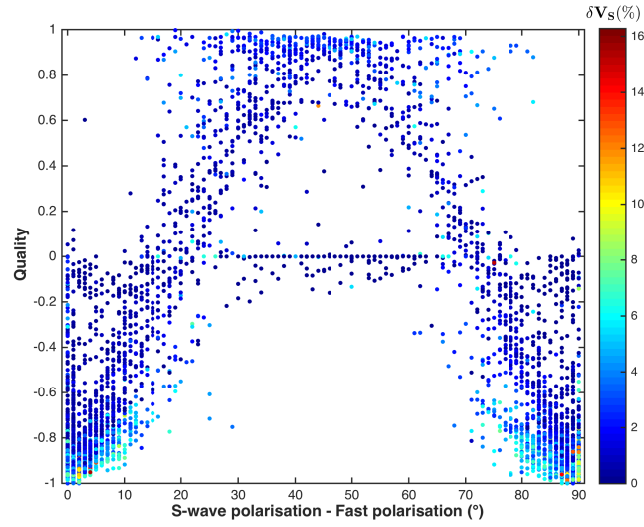
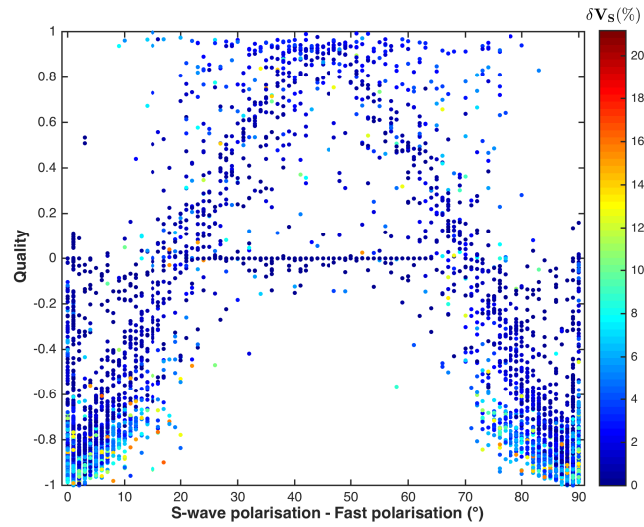


Figure 4: Histogram of azimuth and inclination of the good SWS for the single and double fracture sets.



(a) Single fracture



(b) Double fracture

Figure 5: The SWS quality versus difference between initial source polarisation and the fast S-wave polarisation (ϕ) in the S-plane for the whole dataset. The colour depicts the percentage of shear-wave splitting δV_S . Note that the colour scales are not normalised between the two models.

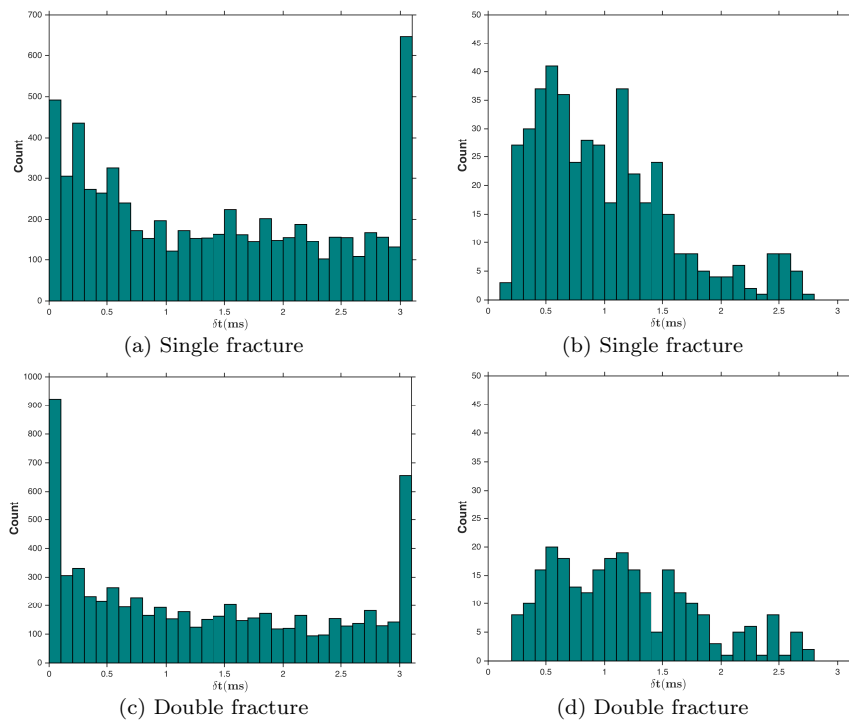


Figure 6: Histogram of δt for the whole dataset for the single (a) and double (c) fracture set models (6624 measurements) as well as for the good SWS results ($Q \geq 0.75$) for the single (b) and double (d) fracture set models. .

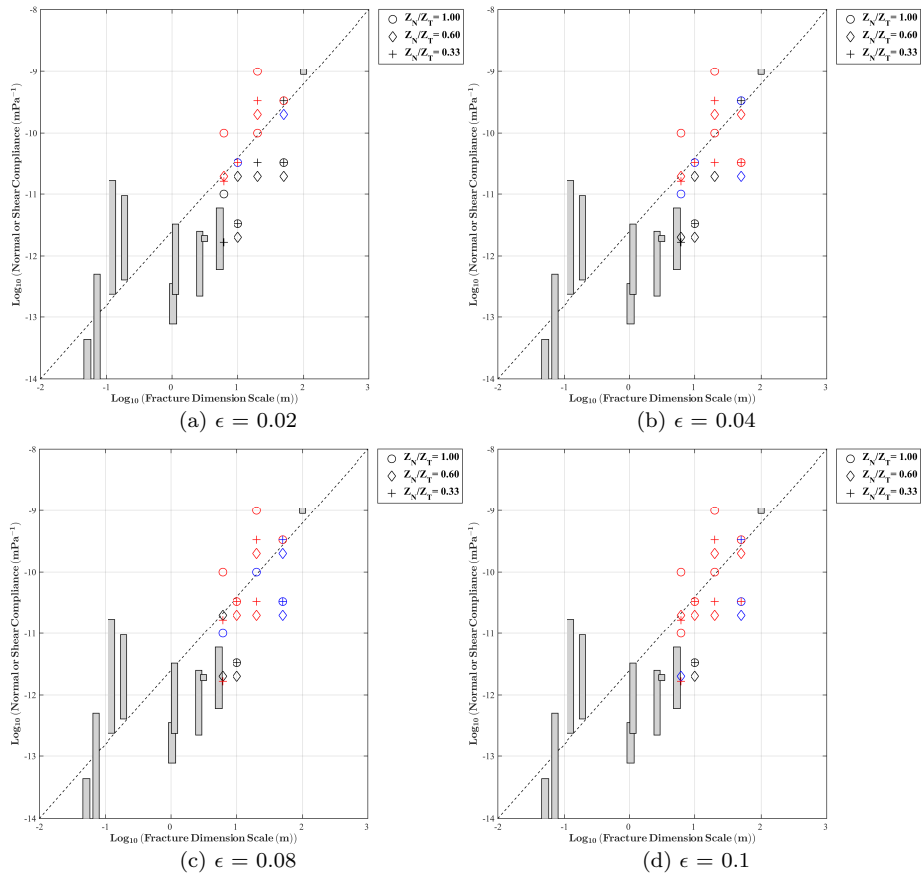


Figure 7: Normal compliance (i.e., inverse stiffness) against fracture size. The grey rectangles are data taken from literature while the other symbols are data from this study. The colour depicts the quality of SWS: good (red); unstable (blue); no SWS (black).

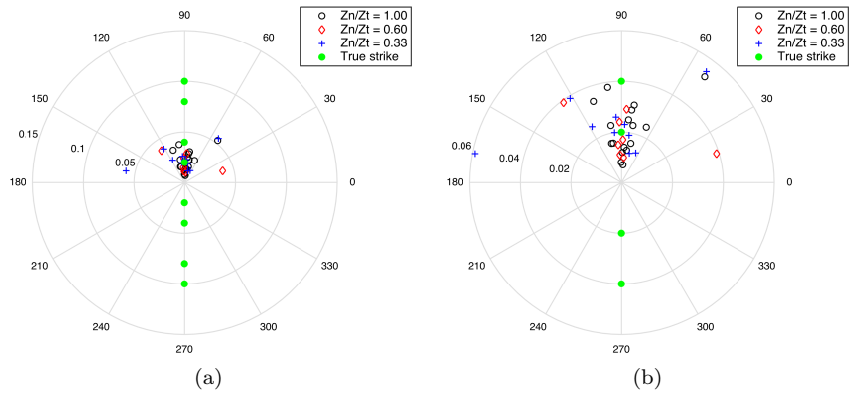


Figure 8: Inversion results for fracture strike versus fracture density for the single fracture set models in the polar plot diagram (left) and zoom in for clear visualisation of the results (right).

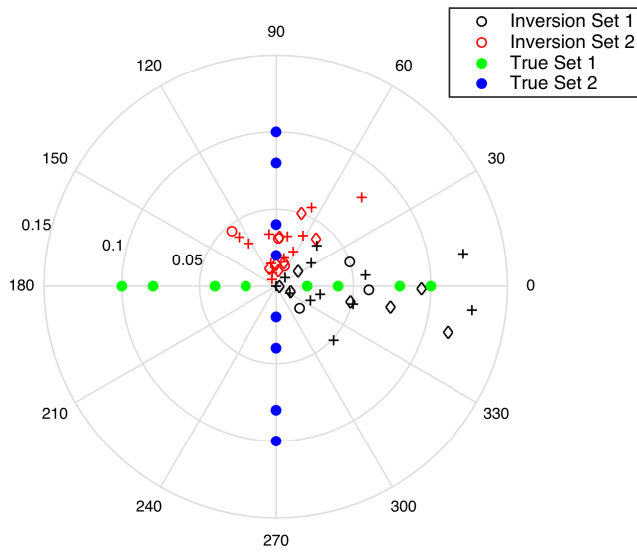


Figure 9: Inversion results for fracture strike versus fracture density for the double fracture set models in polar diagram.

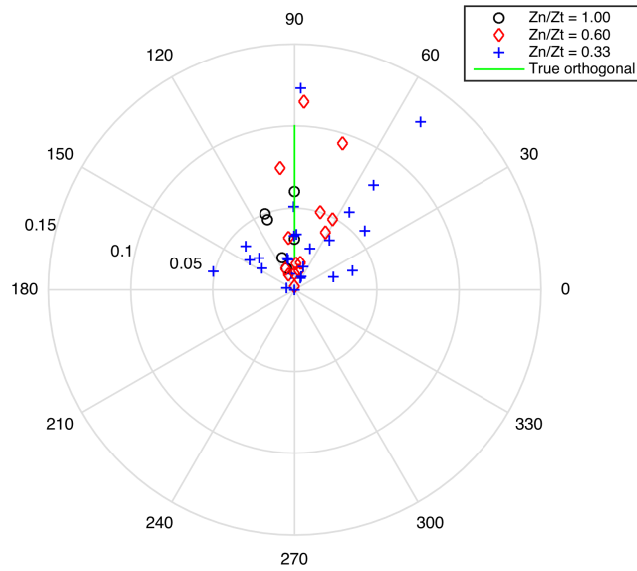


Figure 10: The results of difference in fracture strike inversion for the double fracture sets of in the polar coordinate for the $Z_N/Z_T=1.00, 0.60$ and 0.33 . The radial axis and the angular axes are the fracture density and fracture strike respectively.

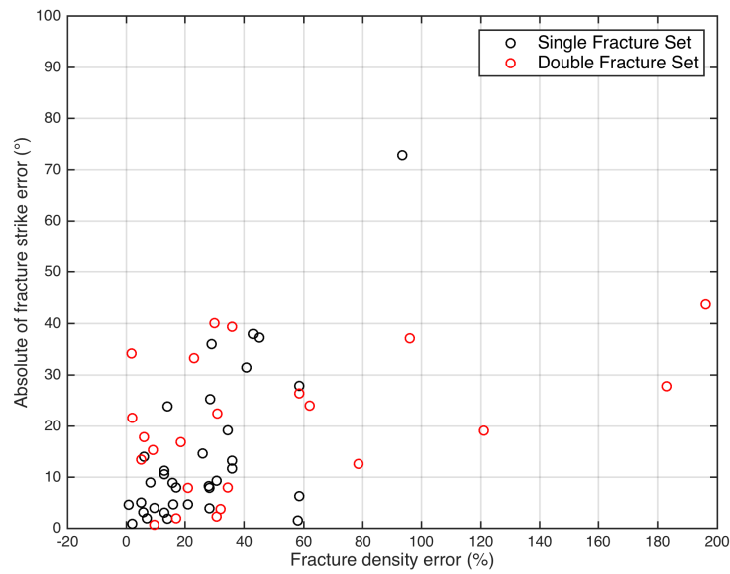


Figure 11: Comparison of inversion results for fracture strike versus fracture density for both the single and double fracture set models.